# Destruction of long-range order recorded with *in situ* small-angle x-ray diffraction in drying colloidal crystals

A. V. Petukhov
*Van 't Hoff Laboratory for Physical and Colloid Chemistry, Debye Institute, University of Utrecht, Padualaan 8, 3584 CH Utrecht, The Netherlands*

I. P. Dolbnya
*DUBBLE CRG/ESRF, The Netherlands Organisation for Scientific Research, ESRF, Boîte Postale 220, F-38043, Grenoble Cedex, France*

D. G. A. L. Aarts and G. J. Vroege
*Van 't Hoff Laboratory for Physical and Colloid Chemistry, Debye Institute, University of Utrecht, Padualaan 8, 3584 CH Utrecht, The Netherlands*

(Received 7 August 2003; published 23 March 2004)

High-resolution synchrotron small-angle x-ray diffraction is applied to characterize the structure and long-range order in a sedimentary hard-sphere colloidal crystal before and during its drying. The principles of the technique and the influence of the coherence properties of the x-ray beam are discussed in detail. The capillary forces generated during the drying process are shown to destroy the long-range order and to break the crystal into smaller crystallites with slightly different orientations. The diffraction is shown to switch from the dynamic regime in the long-range-ordered crystal to nearly kinematic diffraction in the mosaic (short-range-ordered) crystal.

DOI: 10.1103/PhysRevE.69.031405 PACS number(s): 82.70.Dd, 42.70.Qs, 61.10.−i

## I. INTRODUCTION

Suspensions of hard-sphere colloids display a fluid-solid transition at volume fractions above 50%, which is driven by the excluded-volume entropy favoring macroscopically ordered close-packed crystal structures [1,2]. This phenomenon serves as a simple model of crystallization in atomic and molecular systems [1–12]. Recently, self-assembled colloidal crystals have also attracted significant attention as templates for inexpensive large-scale fabrication of photonic band gap materials [13–17]. The order parameters in a colloidal crystal are of great interest from a fundamental point of view and crucial for potential applications. In a so-called *perfect* three-dimensional crystal the long-range order is not destroyed by thermal fluctuations of the atomic positions and their positional correlations extend over the whole crystal size [18]. However, most crystals are imperfect since various extended defects or crystal deformations caused by external or internal (defect-induced) stress fields can easily destroy the positional correlations on large distances.

Diffraction techniques can directly address the crystalline structure and long-range order. Well-collimated synchrotron x-ray beams allow one to obtain clear diffraction patterns from colloidal crystals within a wide range of reciprocal space [19–24]. Moreover, we have recently demonstrated [23] that the extreme flatness of the Ewald sphere at small diffraction angles allow one to achieve resolution in reciprocal space in the *longitudinal* direction beyond $10^{-6}$ of the x-ray wave vector in a single-crystal diffraction scheme with partially coherent synchrotron radiation. By performing small tilts of the single colloidal crystal around one of the low-index orientations, one can then probe the intrinsic width of the reciprocal lattice reflections, which is determined by the extent of the long-range positional order $\Lambda$ on distances over thousand lattice periods. Furthermore, we have found [24] that in a long-range-ordered colloidal crystal diffraction can switch from the kinematic to the dynamic regime. In random-stacking crystals dynamic diffraction manifests itself in an unusual way as the appearance of secondary Bragg rods [24].

This paper focuses on several different, but closely related issues. One of them deals with a further development of the high-resolution small-angle x-ray diffraction technique. We present a thorough analysis of effects of the finite beam coherence on the reciprocal-space resolution of the setup. In particular, we consider limitations of the longitudinal resolution originating from the angular spread of plane-wave components (Sec. III), which was left out earlier [23]. Furthermore, we report on achievement of the setup resolution in the *transverse* direction that is by nearly one order of magnitude higher than that in Refs. [19–24]. This improvement is complementary to the extremely high resolution in the longitudinal direction. The technique is applied for a detailed analysis of the structure and order parameters in a wet sedimentary colloidal crystal (Sec. IV). We demonstrate how one can address the width of the diffraction peaks on three different levels of sensitivity from a single diffraction pattern measured with a fixed crystal orientation.

To further illustrate the strength of the high-resolution small-angle x-ray diffraction technique, we apply it to record *in situ* the destruction of the long-range order during drying (i.e., solvent evaporation from the colloidal crystal). Such drying can be needed if a colloidal crystal is used as a template for a photonic band gap material [13–15,20]. The capillary forces are very strong on the colloidal scale and can play a significant role. For example, their impact was earlier studied in connection with formation of a paint film on surfaces [25]. Capillary forces are also used [16,17,26] to as-

 

semble colloidal particles on a flat substrate. However, the effect of solvent evaporation on the three-dimensional crystal structure was not addressed in the past. For a drying colloidal system x rays are particularly advantageous since optical techniques are not suited due to a great enhancement of the sample turbidity. As will be demonstrated, the long-range order is destroyed during drying. These results (Sec. V) form another important message of this paper.

Finally, the third message of the paper is related to the dynamic character of x-ray diffraction in colloidal crystals (Sec. VI). A direct comparison of the intensity of diffracted beams with that of the (remaining) direct beam is performed. It unambiguously supports the interpretation of the secondary Bragg rods in Ref. [24] as multiple x-ray scattering. Moreover, the strength of the diffraction is shown to drastically reduce after destruction of the long-range order, which can now be seen as a sum of nearly kinematic diffraction patterns from small crystallites in the mosaic.

## II. EXPERIMENTAL SECTION

Spherical silica colloids [27] were synthesized and coated with 1-octadecanol to provide sterical stabilization. Their diameter of 224 nm was derived from small-angle x-ray scattering in a dilute suspension (the form factor). This value was found to agree with results of static and dynamic light scattering (230 nm) and sedimentation (218 nm) experiments [28]. A size polydispersity of 4.1% was determined by transmission electron microscopy. The particle density was established at 1.69 g/ml [28], which is lower than that of bulk silica due to porosity. Cyclohexane has a specific weight of 0.77 g/ml and is very volatile. The colloidal particles act as hard spheres in this solvent [29]. Nonadsorbing polydimethylsiloxane polymer (molecular weight 91.7 kg/mol, $M_w/M_n=1.9$, radius of gyration $R_g=14$ nm) was added to the suspension to accelerate crystallization of large colloidal crystals [23].

Samples were prepared in long (100 mm) flat glass capillaries with internal cross section of $0.2\times 4$ mm$^2$, which were filled with a dilute suspension (where 5% and 10%–15% of the volume are filled by colloid and penetrable polymer coils, respectively). Capillaries were stored upright before and during the experiment. The colloidal particles sediment within about a week. Colloidal crystals nucleated after the sedimentation was complete at the top of the sediment and grew downwards as was observed by Bragg reflections of visible light. After a few weeks the crystallization stopped and the bottom part of the sediment remained amorphous. The height of the crystalline part of the sediment was about 5 mm.

A small-angle x-ray diffraction study (SAXS) was performed at the SAXS/WAXS station of the BM-26B Dutch-Belgian beam line (DUBBLE) at the European Synchrotron Radiation Facility (ESRF) in Grenoble [30]. The horizontal and vertical primary slits situated at a distance $z_{H1}=28$ m from the bending magnet radiation source determine the angular divergence of the synchrotron radiation beam. Slit widths down to $100\times 100$ $\mu$m$^2$ were used. Monochromatic 15 keV x-rays (wavelength $\lambda=0.83$ Å, spectral width $\Delta\lambda/\lambda=2\times 10^{-4}$) were selected by a sagittally focusing (i.e., in the horizontal plane of the electron orbit) double-crystal Si(111) monochromator, located at $z_{mono}=33$ m. It was followed by a bent silicon mirror at $z_{mir}=35.5$ m downstream from the source, which focused the beam in the vertical plane and discriminated against harmonics coming from the monochromator. The harmonic suppression coefficient was about $10^{-3}$. The parasitic small-angle scattering originating from the x-ray optical elements was blocked by two sets of slits installed at $z_{H5}=42$ m and $z_{H6}=48$ m.

The sample was mounted at $z_{samp}=49$ m on computer-controlled rotation and translation stages allowing us to scan through the sediment and to carefully orient the colloidal single crystals. The diffraction was recorded at a distance of 8 m from the sample ($z_{det}=57$ m) by an x-ray sensitive CCD (charge-coupled device) camera (X-Quis, Photonics Science). The diffraction image was digitized into $1024\times 1024$ pixels with the pixel size corresponding to 52 $\mu$m physical separation on the phosphor screen of the camera. The entire field of view was about 7.5 cm along the diagonal. The readout offset was about 32 counts per pixel with a typical noise of two to three counts. The maximum measurable intensity corresponded to 4096 counts per pixel (12 bit). Moreover, significant efforts were spent on a careful alignment of all optical elements of the setup. The direct beam was focused on the screen of the CCD camera. As is shown in Sec. IV, a significant improvement of the transverse resolution has been achieved, which is close to the theoretical limit for the optical scheme of BM26B. This achievement was crucial for the results presented in Sec. V. The sample drying was also visually observed using a video camera installed in the experimental hutch.

## III. TRANSVERSE AND LONGITUDINAL COHERENCE

Diffraction appears as a result of coherent summation of waves scattered by different colloidal spheres. It can reveal the positional correlation of the particles only if the waves scattered by them are able to interfere. This implies certain requirements for the beam coherence, which are considered in this section for the small-angle diffraction geometry. Coherent properties of an x-ray beam are different in the transverse and longitudinal directions. Correspondingly, one should distinguish the resolution of a small-angle diffraction setup in two different directions, which are denoted as the transverse and longitudinal resolution in the following. The former determines the ultimate limit of the apparent size of each reflection in the detector plane. The latter can be exploited in single-crystal diffraction [23].

The incident wave inside the sample is a result of incoherent summation of waves independently emitted by various points of the spatially extended x-ray source of a size $d_s$. For a freely propagating wave the phase front possesses random corrugation, which becomes comparable to the x-ray wavelength $\lambda$ on distances of the order of the transverse coherence length

$$l_{tr}=\lambda z/d_s, \tag{1}$$

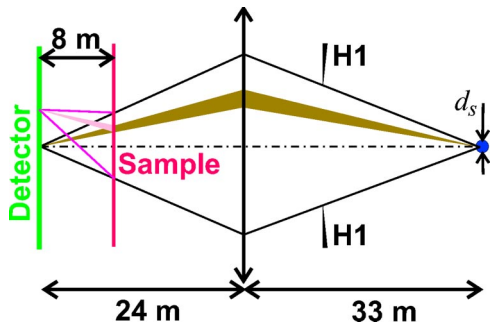


FIG. 1. (Color online) Sketch of beam focusing within the optical setup. H1 denotes the entrance slits. Indicated distances correspond to the position of the second crystal of the monochromator, which performs focusing in the horizontal direction. The shaded areas schematically denote one of the cones, where the radiation is spatially coherent. A diffracted beam is shown in a different color.

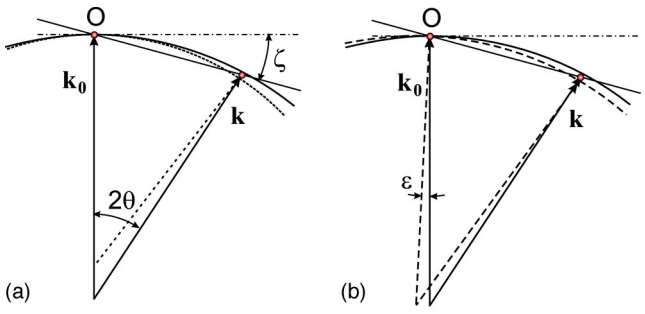


FIG. 2. Ewald sphere construction for a parallel beam with a finite spectral width $\Delta\lambda$ (a) and for a monochromatic beam with a finite angular spread $\epsilon$ of plane-wave components in the incident beam (b). The angles are greatly exaggerated for clarity. The small circles denote the origin of the reciprocal space of the sample O and an $(hkl)$ reciprocal lattice reflection. $2\theta$ is the diffraction angle, $\zeta$ is the sample tilt angle.

which increases with the distance $z$ traveled by the beam from the source. With the source size of about $d_s=100$ $\mu$m (root mean square) at the ESRF and at the wavelength $\lambda$ used in the present experiment, the coherence length is $l_{\mathrm{tr,\,mono}}=27$ $\mu$m at the position of the monochromator and $l_{\mathrm{tr,\,mir}}=30$ $\mu$m at the mirror. After a focusing element the beam converges and, correspondingly, the transverse coherence length $l_{\mathrm{tr}}$ shrinks as illustrated in Fig. 1. Assuming ideal optical elements, at the sample position $l_{\mathrm{tr}}$ can be estimated as $l_{\mathrm{tr},h}=l_{\mathrm{tr,\,mono}}(z_{\mathrm{det}}-z_{\mathrm{samp}})/(z_{\mathrm{det}}-z_{\mathrm{mono}})=9$ $\mu$m and $l_{\mathrm{tr},v}=l_{\mathrm{tr,\,mir}}(z_{\mathrm{det}}-z_{\mathrm{samp}})/(z_{\mathrm{det}}-z_{\mathrm{mir}})=11$ $\mu$m in the horizontal and the vertical directions, respectively.

Results presented in the following section show that in the horizontal direction a transverse coherence length $l_{\mathrm{tr}}>6$ $\mu$m was indeed reached in our experiment, suggesting practically ideal performance of the beam line optics. Colloidal spheres separated in the transverse direction by a distance larger than $l_{\mathrm{tr}}$ are irradiated by mutually incoherent waves and their scattering fields do not interfere. As a result, the transverse coherence was sufficient to resolve the diffraction peaks ($l_{\mathrm{tr}}$ is larger than the structure period), but is far too small to probe the long-range order in the transverse direction.

As was suggested in our previous paper [23], a much higher longitudinal resolution can be achieved since conditions for coherent interference in the longitudinal direction can be fulfilled on much larger distances. By tilting the single crystal to a small angle $\zeta$ and, for example, observing the variation of the total intensity $I_{(hkl)}(\zeta)$ of a particular $(hkl)$ reflection, one can then exploit the coherent interference between waves scattered at the front and rear side of the sample [23] to resolve the intrinsic width of the reciprocal lattice reflections. The limiting factors here are related to the finite spectral width $\Delta\lambda$ of the radiation [23] and the finite angular spread of the plane-wave components. The first effect is illustrated by the Ewald sphere construction in reciprocal space shown in Fig. 2(a). A spread in the wavelengths $\lambda$ in the incoming beam leads to a series of Ewald spheres with slightly different curvatures, which all must pass through the origin O of the reciprocal space of the sample. The finite bandpass $\Delta\lambda$ can thus reduce the resolution of the scheme for measurements of the rocking curve $I_{(hkl)}(\zeta)$. From the construction in Fig. 2(a) one can find that at small angles the resolution in the reciprocal space is limited by

$$\delta q_1=\frac{2\pi\Delta\lambda}{\lambda^2}2\theta^2 \tag{2}$$

in agreement with the result of an earlier consideration in real space [23]. For instance, for the (110) reflections, $2\theta_{(110)}=7\times10^{-4}$ rad in our case so that $\delta q_1\sim0.004$ mm$^{-1}$.

Reduction of the longitudinal resolution, which is related to the angular spread $\epsilon$ of the plane-wave components in the x-ray beam inside the sample, is illustrated in Fig. 2(b). The corresponding spread of the Ewald spheres for $\theta\ll1$ and $\epsilon\ll1$ limits the resolution to

$$\delta q_2=\frac{2\pi}{\lambda}2\theta\epsilon. \tag{3}$$

We note that $\delta q_2$ also reduces towards small scattering angles, although only linearly with $\theta$. One could distinguish two contributions to the *total* value of $\epsilon$. One of them is related to the fact that the x-ray beam hitting the sample has the form of a cone converging towards the detector. The opening angle of this cone $\epsilon_{\mathrm{cone}}$ is determined by the acceptance angle of the primary slits divided by the magnification factor of the focusing system. For 100 $\mu$m wide slits one can evaluate $\epsilon_{\mathrm{cone}}=5\times10^{-6}$ and $6\times10^{-6}$ in the horizontal and the vertical directions, respectively. The other contribution arises from the finite transverse coherence of the x-ray beam, which is discussed above. As a result, at a given point in the beam there is a finite angular spread $\epsilon_{\mathrm{tr}}=\lambda/l_{\mathrm{tr}}$ of the mutually incoherent plane waves. Assuming uncorrelated contributions of $\epsilon_{\mathrm{cone}}$ and $\epsilon_{\mathrm{tr}}$, one can estimate the total angular spread $\epsilon$ of the plane-wave components as $\sqrt{\epsilon_{\mathrm{tr}}^2+\epsilon_{\mathrm{cone}}^2}$, which amounts to $1.05\times10^{-5}$ and $0.95\times10^{-5}$ rad in the horizontal and the vertical plane, respectively.

Using the estimates given above and Eq. (3), one gets for the (110) reflections $\delta q_2=0.28$ mm$^{-1}$ and 0.25 mm$^{-1}$ in the

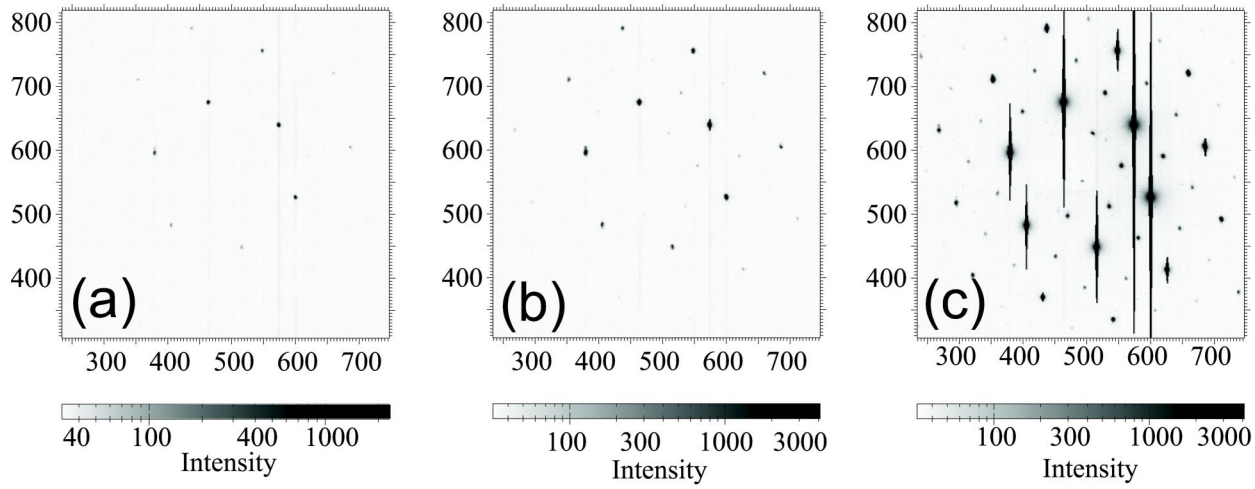


FIG. 3. Diffraction patterns measured with the x-ray beam incident along the [001] direction. The exposure time of the CCD camera is $\Delta T=0.1$ s (a), $\Delta T=1$ s (b), and $\Delta T=60$ s (c). Throughout this paper the intensities are displayed in as-read detector counts without subtracting the background ($\sim 32$ counts).

horizontal and vertical directions, respectively. One can see that $\delta q_2 \gg \delta q_1$, i.e., $\delta q_2$ is a much more important limiting factor than $\delta q_1$, considered earlier [23]. Yet, the main conclusion of Ref. [23] is not affected. For partially coherent synchrotron radiation the very flat nature of the Ewald sphere leads, in principle, to a longitudinal resolution $\delta q/k_0$ better than $10^{-8}$ for a low-order reflection. This would allow one to probe positional correlations in the particle positions on distances up to $2\pi/(\delta q_2)>1$ cm along the beam propagation direction. However, as further discussed in Sec. VI, there is another limitation of the technique related to the switch of the diffraction into the dynamic regime on distances of the order of 100–200 $\mu$m, which further limits the effective longitudinal resolution in the present case to about $\delta q/k_0 \sim 10^{-6}$.

## IV. STRUCTURE AND LONG-RANGE ORDER OF THE WET CRYSTAL

Figure 3 displays diffraction patterns measured in a crystal with its hexagonal planes (nearly) parallel to the capillary walls. The hexagonal planes of the crystal were carefully aligned normal to the incident x-ray beam. The images are obtained at different exposure times $\Delta T$. In panel (a) $\Delta T=0.1$ s and only the brightest reflections are visible. Upon increase of $\Delta T$ in panels (b) and (c) the weaker reflections become detectable while the brightest reflections greatly oversaturate the CCD camera. In (c) the too high exposure also leads to the appearance of vertical stripes in the image, presumably caused by a charge spill-out effect into neighboring pixels in the vertical direction. By performing such a series of measurements one can compensate for the limited dynamic range of the CCD camera (i.e., the ratio of the maximum and minimum intensities, which can be reliably measured within one diffraction pattern).

The pattern in Fig. 3 is typical for a random hexagonal close-packed (rhcp) structure, which was demonstrated earlier [23,24] in this system. Moreover, it is a very common long-living metastable structure for colloidal spheres with a hard-core interaction potential [5,22–24,31–38]. We adopt the usual $(hkl)$ Miller indices for the reciprocal lattice reflections of an rhcp crystal [23]. In Fig. 3 $l\approx 0$ and one can see two types of reflections with one-third of the reflections being very much brighter. These are the stacking-independent $(hk0)$ reflections with $h-k$ divisible by 3, where contributions of all crystal planes interfere constructively [23]. The other, weaker $(hk0)$ reflections with $h-k$ not divisible by 3 appear when the stacking-disorder-induced Bragg rods [22–24,34,39] cross the Ewald sphere.

Figure 4 presents the horizontal profile of one of the (110)-type diffraction peaks in Fig. 3(a). The solid line is a Gaussian fit $I(q_x)=I_0 \exp[-(q_x-q_{x,0})^2/(2\sigma^2)]+I_{\mathrm{dark}}$ with $I_0$ and $I_{\mathrm{dark}}$ denoting the maximum peak intensity and the readout offset, respectively, $q_{x,0}=600.8$ detector pixels is the $x$ position of the peak and the standard deviation is $\sigma=1.1$ pixels $=0.5$ $\mu\mathrm{m}^{-1}$. As demonstrated below, the crystal has

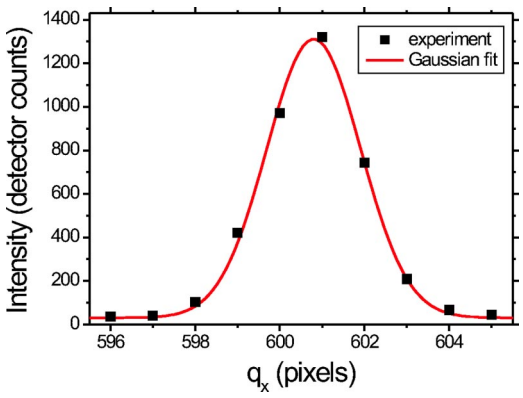


FIG. 4. Horizontal profile through the (110)-type diffraction peak in Fig. 3(a) [with the maximum intensity at the detector coordinates $(x,y)=(601,527)$]. Points present the detector readings and the solid line is a Gaussian fit as described in the text. The distance between pixels corresponds to about 0.47 $\mu\mathrm{m}^{-1}$.

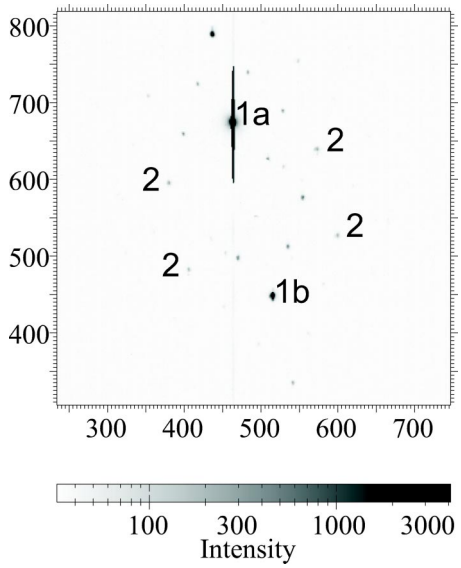


FIG. 5. Diffraction pattern from a slightly tilted sample. The exposure time is $\Delta T = 10$ s. The six (110)-type reflections are marked by 1a, 1b, or 2. $t = -35$ min.

extremely narrow reflections so that the peak width $2\sigma$ is entirely limited by the instrument. In addition to the finite transverse coherence length of the beam $l_{\mathrm{tr}}$ discussed above, the peak can be further broadened by the resolution of the CCD detector itself and the imperfectness of focusing of the beam at the detector plane depending on the quality of the optical elements and their alignment. Yet, from the peak width $2\sigma$ in Fig. 4 one can conclude that at least $l_{\mathrm{tr}} > 2\pi/(2\sigma) = 6$ $\mu$m in the horizontal direction. The vertical profile through the same reflection is $\sim 20\%$ broader possibly due to abberations of the mirror that focuses beam vertically. All the other reflections in Fig. 3 have the same slightly elliptical shape with the same widths.

Another way to demonstrate that the peak width in Fig. 4 is close to the theoretical resolution limit of the optical scheme of the beam line is as follows. The smallest achievable horizontal size of the reflections within the detector plane is simply governed by the source size $d_s$ times the magnification factor $(z_{\mathrm{det}} - z_{\mathrm{mono}})/z_{\mathrm{mono}} = 24/33 = 0.73$ of the focusing optics. The achieved physical width $2\sigma = 114$ $\mu$m of the reflection in Fig. 4 is only a factor of 1.6 larger than the theoretical limit assuming $d_s = 100$ $\mu$m.

To make use of the higher resolution achievable along the longitudinal direction in a small-angle experiment (see the discussion in Sec. III), the sample was tilted by $\zeta = 0.4°$ with respect to its orientation in Fig. 3. The axis of rotation is slightly inclined (by about 15° counterclockwise) from the vertical direction. The resulting diffraction pattern is shown in Fig. 5. In this case the Bragg condition is still (nearly) fulfilled for two (110)-type reflections, which leads to only two very bright diffraction peaks strongly oversaturating the detector in Fig. 5 (marked in the figure with 1a and 1b). The other four (110)-type reflections (marked in the figure with 2) miss the Ewald sphere by $\Delta q = \zeta q_{(110)} = 0.3$ $\mu\mathrm{m}^{-1}$ and their intensity is strongly reduced (by about three orders of magnitude). Here $q_{(110)} = 4\pi/a$ denotes the wave vector of the

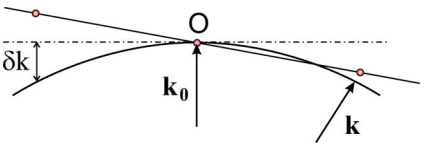


FIG. 6. Illustration of the asymmetry of the diffraction patterns in Figs. 3 and 5 originating from the curvature of the Ewald sphere. The small circles denote the origin of the reciprocal space of the sample O and two opposed $(hkl)$ and $(\overline{hkl})$ reciprocal lattice reflections, $\delta k$ is the deviation of the Ewald sphere from a plane. The wave vector of the incident beam $\mathbf{k}_0$ slightly misses the $[hkl]$ crystallographic direction.

(110) reciprocal lattice reflection, corresponding to an arrangement of spheres with a period of half the nearest-neighbor distance $a$. Thus, the width of the reflections $\delta q$ must be very much smaller than the wave vector mismatch $\delta q \ll \Delta q$.

A further estimate of the width of the reflections $\delta q$ can be obtained by noting that the diffraction patterns in Figs. 3 and 5 display strong asymmetry, i.e., the intensities of two opposed reflections $(hkl)$ and $(\overline{hkl})$ are significantly different [e.g., the (110)-type reflections marked 1a and 1b in Fig. 5]. At a small diffraction angle $2\theta$ the Ewald sphere deviates from a plane by as little as $\delta k = k_0 2\theta^2$, as illustrated in Fig. 6. For a pair $(hkl)$ and $(\overline{hkl})$ of opposed reflections the difference in the wave vector mismatch cannot be larger than $2\delta k$. The strong asymmetry of the (110)-type reflections thus suggests that $\delta q < 2\delta k_{(110)} = 0.037$ $\mu\mathrm{m}^{-1}$. This result indicates the presence of long-range order over distances of the order of $2\pi/(2\delta k_{(110)}) \approx 200$ $\mu$m, i.e., over the thickness of the capillary in agreement with our earlier result [23]. In other words, the crystal before drying does possess long-range order, i.e., positional order over the whole crystal size.

In the following section we present the results of the *in situ* observation of the modification of the order parameters in the crystal during its drying. To make use of the high longitudinal resolution, which can be obtained in small-angle diffraction, a slightly tilted sample orientation, used in Fig. 5, was chosen. In this case we can address the width of the diffraction peaks on three different levels of sensitivity. The direct determination of the peak width from the detector image is the most crude and can detect broadening of the reciprocal lattice reflections in the transverse direction only of the order of $2\sigma = 1$ $\mu\mathrm{m}^{-1}$. In the longitudinal direction a much higher sensitivity can be achieved. One can make use of the tilted crystal orientation and compare the intensities of the (110)-type diffraction peaks marked 1 and 2, respectively, in Fig. 5. In this way one can detect changes of the width of the reflections, when it is comparable to $\Delta q = 0.3$ $\mu\mathrm{m}^{-1}$. The highest sensitivity $\sim 2\delta k_{(110)} = 0.037$ $\mu\mathrm{m}^{-1}$ can be achieved by watching the asymmetry of the diffraction pattern (i.e., by comparing the intensities of the reflections 1a and 1b).

## V. DRYING: LOSS OF LONG-RANGE ORDER

The drying was achieved by cutting off the top part of the capillary with supernatant. Cyclohexane was allowed to

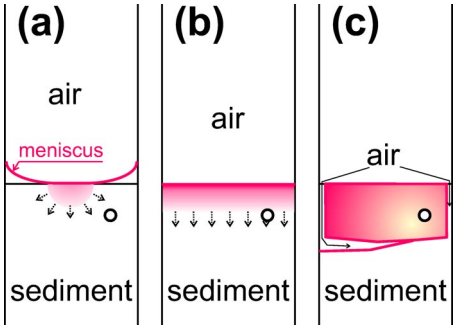


FIG. 7. Sketch of some of the visually observed stages during drying, when the meniscus reaches the sediment (a), flattens out completely (b), and air penetrates into the sediment (c). These three stages approximately correspond to diffraction patterns shown in Figs. 8, 9, and 11, respectively. The approximate position of the observation point within the sediment is marked by a circle.

evaporate from the remaining short ($\sim$30 mm) part of the capillary through the open top. Figure 7 schematically summarizes some of the important stages of the drying process as observed using the video camera. Photographs taken from the TV screen are available at an Internet page, which supplements this paper [40].

No significant change of the diffraction pattern was detected after opening the capillary, when the meniscus was well above the sediment. In fact, the pattern in Fig. 5 was taken when the capillary was already opened and the solvent was evaporating. The same pattern was measured in the closed capillary at the same sample orientation.

Figure 8 presents the diffraction pattern measured when the meniscus touched the sediment [as sketched in Fig. 7(a)]. To indicate the time scale in the following, this moment of time is used as $t=0$. The pattern in Fig. 5 was taken 35 min before $t=0$. The pattern in Fig. 9 was taken at about $t=14$ min, when the meniscus flattened while the sediment was still wet [see Fig. 7(b)]. The intensity of the brightest

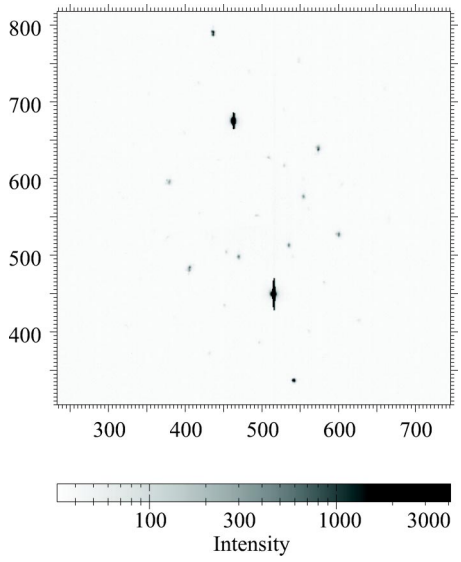


FIG. 8. Diffraction pattern measured when meniscus touches the sediment ($t=0$). The exposure time is $\Delta T=10$ s.

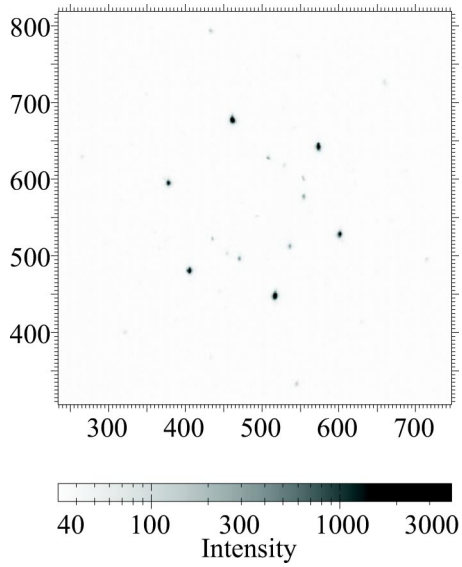


FIG. 9. Diffraction pattern measured when meniscus becomes flat ($t=14$ min). The exposure time is $\Delta T=10$ s.

two (110)-type reflections is now significantly reduced, while the other four are strengthened, leading to a (nearly) sixfold symmetric pattern. Now the reflections 2 are only a factor 2 to 2.5 weaker than reflection 1a and 1b.

The origin of the modification of the diffraction patterns in Figs. 5, 8, and 9 is illustrated in Fig. 10. For a long-range-ordered crystal in Fig. 5 the reflections are very narrow (solid line in Fig. 10). For the 1a and 1b (110)-type reflections the Bragg condition is (nearly) fulfilled, i.e., the wave vector mismatch is small. Moreover, due to the curvature of the Ewald sphere there is a difference between their intensities in Fig. 5. For the other four (110)-type reflections the wave vector mismatch $\Delta q$ is relatively large so that these reflections are nearly invisible. Upon shortening of the positional order, the reflections broaden (dashed line in Fig. 10) leading to a strong reduction of the intensity of reflections 1a and 1b in Fig. 8. We note also that the asymmetry of the pattern has disappeared in Fig. 8, which indicates that the width of the reflections is now $\delta q > \delta k_{(110)}$. Yet, since two (110)-type diffraction peaks (reflections 1a and 1b) are still much stronger than the other four (reflections 2), $\delta q$ is smaller than the

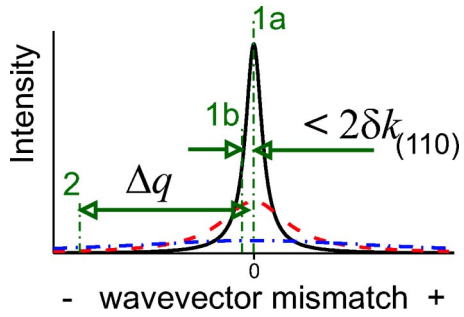


FIG. 10. Qualitative illustration of the modifications of the intensities of (110)-type reflections in Figs. 5 (solid line), 8 (dashed), and 9 (dot-dashed), which are induced by their broadening. Vertical lines denote the wave vector mismatch for reflections 1a, 1b, and 2.

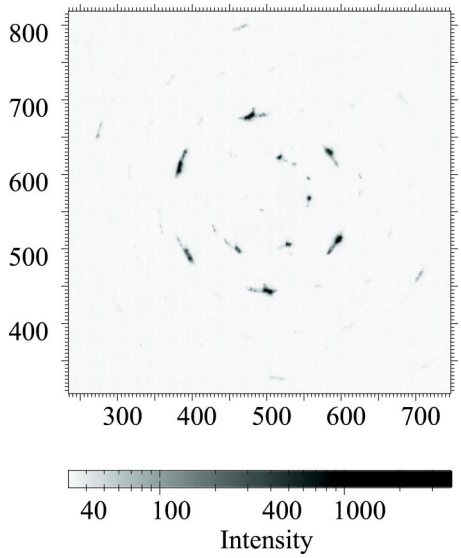


FIG. 11. Diffraction pattern measured when air penetrated into the sediment ($t=21$ min). The exposure time is $\Delta T=15$ s.

wave vector mismatch $\Delta q$ induced by the sample tilt. Upon further increase of the capillary-force-induced strain field, the width of the reflections becomes comparable to the tilt-angle-induced wave vector mismatch $\Delta q$ (dot-dashed line in Fig. 10), so that the intensities of all six reflections of the (110)-type in Fig. 9 are similar. This broadening could be explained by shortening the spatial extent of the positional order $\Lambda$ down to about $2\pi/\Delta q=20$ $\mu$m.

We note that our resolution in the plane of the detector is still too low to resolve the broadening of the reciprocal lattice reflection. The reflections in Figs. 5, 8, and 9 keep practically the same shape and width. We should further mention that the stress field may somewhat change the crystal orientation and, thus, affect the wave vector mismatch $\Delta q$ and the symmetry of the pattern (compare with Fig. 3). However, it is necessarily accompanied by a significant broadening of the reflections since their intensity is now very much weaker.

The pattern in Fig. 11 was taken $t=21$ min after the pattern in Fig. 8. At this moment the meniscus turned upside down and air penetrated down along the sides of the capillary [as sketched in Fig. 7(c)]. Formation of a large air void in the sediment was visually observed on the TV screen connected to the video camera in the experimental hutch. The diffraction peaks are seen to split into many separate reflections in Fig. 11 indicating that the crystal is not able to withstand a too strong stress anymore and it breaks up into smaller crystallites. Note that the peak broadening was observed only in the azimuthal direction. As illustrated in Fig. 12, the radial profile kept practically the same instrument-limited width as in Fig. 4. The latter result suggests that the crystallites in the mosaic are significantly larger than, and possess positional order over distances more than, the x-ray beam transverse coherence length $l_{tr}>6$ $\mu$m (see the discussion of Fig. 4). The azimuthal broadening, in turn, is related to a reduction of the orientational correlation between different crystallites in the mosaic.

After $t=21$ min formation of further voids in the sediment was visually observed [40]. At $t\approx 28$ min the sediment became turbid and looked dry. However, no remarkable changes of pattern was observed up to $t=30$ min, suggesting that the observation point was still wet. Its final drying was observed only between $t=30$ and $t=35$ min as a significant increase of the diffracted intensity due to an enhancement of the scattering contrast as can be seen in Fig. 13. We note that apart from the increased intensity, the diffraction pattern is very similar to that shown in Fig. 11.

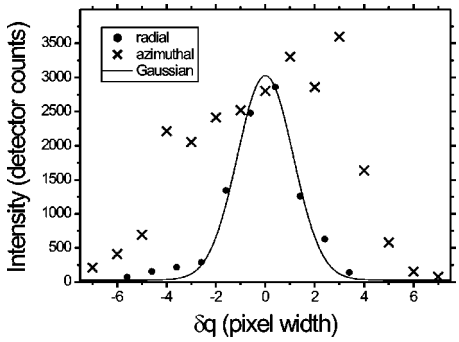


FIG. 12. Radial (circles) and azimuthal (crosses) profiles through the (110)-type diffraction peak in Fig. 11 [around detector coordinates $(x,y)=(600,515)$]. The solid line is a Gaussian function with the same width as in Fig. 4.

Several factors could play a role in the drying process. First of all, solvent evaporation leads to an increase of the concentration of nonabsorbing polymer, which osmotically compresses the sediment. In the case of slow evaporation (giving sufficient time to equilibrate) the system should follow the so-called drying line [41]. In our experiment evaporation of the volatile cyclohexane was presumably too fast for the polymer diffusion into the sediment to equilibrate its concentration. In this case one could expect a permanent increase of osmotic compression at the top of the sediment

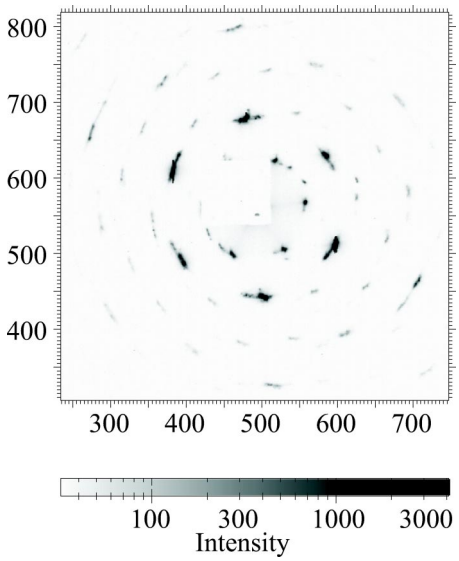


FIG. 13. Diffraction pattern measured in the dry crystal ($t=38$ min). Note the increased contrast. The exposure time is $\Delta T=30$ s.

starting right after the opening of the capillary. However, we did not observe any remarkable effect in the early stage of the solvent evaporation, when the meniscus was well above the sediment. We cannot, however, completely rule out this effect at later stages when the polymer concentration had raised even further.

Fast modification of the diffraction pattern began approximately when the meniscus touched the sediment. As sketched in Fig. 7(a) the capillary forces, which can strongly push the colloidal particles together, can come into play. However, they are applied only at the top of the sediment, at a couple of millimeters distance from the observation point. Our results suggest that the stress fields generated by the pressure differences and the strain at the air-solvent interface are able to elastically propagate over a macroscopically large distance without strong decay (illustrated by arrows and shading in Fig. 7).

Flattening of the meniscus, as sketched in Fig. 7(b), and creation of new air-solvent interfaces inside the sediment as illustrated in Fig. 7(c), increases the area over which the capillary forces act and brings them closer to the observation point. As we have observed, the enhanced stress field leads to further broadening of the crystal reflections followed by a breakup of the single crystal.

Surprisingly, the main effect of the drying was detected at the three stages sketched in Fig. 7 when the drying front did not yet reach the observation region and there were no capillary forces acting within that part of the crystal. On the contrary, the diffraction pattern did not change anymore when the crystal dried out completely, although the colloids at that stage are strongly pushed together by both the capillary forces and the van der Waals attractions (enhanced due to increased refractive index contrast).

We finally remark that to disturb the positional order in an *ideal* single crystal, one has to apply a nonuniform external stress field (e.g., of the bending or screwing type) to the crystal. A *real* crystal, in addition, may contain ''internal'' sources of the local nonuniform stress field. In particular, a colloidal hard-sphere crystal contains a finite density of defects [42] even at thermodynamic equilibrium; much more imperfectness could be induced by numerous growth defects incorporated in the experimental conditions. An additional contribution to lattice disorder might be provided by the polydispersity of the colloidal spheres [43–45]. All these effects could further reduce the ability of a colloidal crystal to sustain compression.

## VI. DYNAMIC DIFFRACTION AND LONG-RANGE ORDER

So far we have used the kinematic approach to describe our results. However, in crystals possessing long-range order the x-ray diffraction can switch to the dynamic regime [24] due to coherent summation of many weak scattered waves upon their propagation in a single crystal. Below we demonstrate a direct relation between the strength of the diffraction and the extent of the positional order. This phenomenon could thus be employed as an alternative approach to study the long-range order in colloidal crystals.

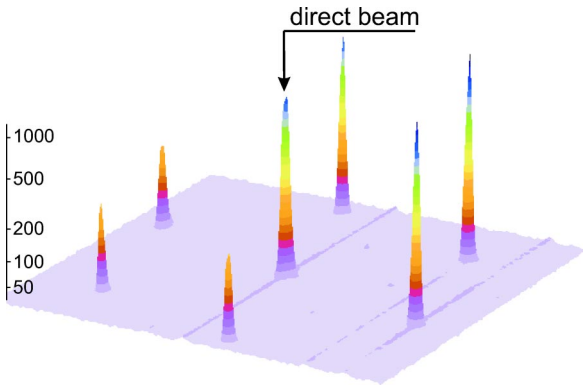


FIG. 14. (Color online) Three-dimensional plot of the central part of the same diffraction pattern as in Fig. 3(a) but measured without beam stop. The exposure time is $\Delta T = 0.1$ s.

To directly demonstrate the dynamic character of the x-ray diffraction in the wet crystal, we show in Fig. 14 a diffraction pattern measured without beam stop. The crystal orientation here is the same as the one used in Fig. 3. Three out of the six lowest-order (110) diffraction peaks are seen to have intensities comparable to that of (the rest of) the direct beam. The other three are somewhat weaker presumably because the incident beam slightly misses the [001] crystallographic direction, which, together with the extremely narrow width of the reflections, leads to an asymmetry of the pattern (see Fig. 6 and Ref. [23]).

The theory of dynamic diffraction in the presence of many mutually interacting waves is rather complex. Instead, one can use the much simpler kinematic approach for an order-of-magnitude estimate of the conditions needed to switch the diffraction into the dynamic regime. We further assume that the crystal of a thickness $L$ along the beam consists of $(\Lambda/L)$ domains, which are positionally uncorrelated with each other. Then, assuming coherent interference over the domain size $\Lambda$ (see Sec. III) but incoherent summation of intensities originating from different domains, the power diffracted into a particular $(hkl)$ reflection obeying the Bragg law can be estimated as

$$P_{(hkl)} = \frac{L\Lambda}{L_{(hkl)}^2} P_0, \tag{4}$$

where $P_0$ is the total power of the direct beam and $L_{(hkl)}$ is a characteristic length describing the strength of the diffraction. In a long-range ordered crystal $\Lambda = L$ and $P_{(hkl)}$ grows quadratically $\propto L^2$ inside the single crystal. For an $(hkl)$ reflection with diffraction vector $q_{(hkl)}$ the characteristic length is given by $L_{(hkl)} = [\lambda n r_0 Z \sqrt{F(q_{(hkl)})}]^{-1}$ [24], where $r_0 = e^2/(mc^2)$ is the Thompson radius, $n$ is the number density of the spheres, $Z$ is the excess number of electrons in the colloidal particle relative to an equivalent volume of solvent, and $F(q)$ is the normalized scattering form factor. For the strong (110) reflections seen in Fig. 14 one can evaluate the characteristic length $L_{(110)}^{\mathrm{wet}} = 0.26$ mm in a wet colloidal crystal. Clearly, the sample thickness $L = 0.2$ mm was comparable to $L_{(110)}^{\mathrm{wet}}$, so that the diffracted beams must signifi-

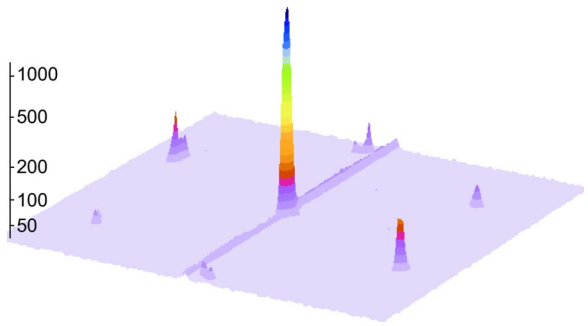


FIG. 15. (Color online) Three-dimensional plot of the central part of a diffraction pattern measured without the beam stop in the dry crystal ($t=55$ min). The exposure time is $\Delta T=0.05$ s. The small "ridge" in the background level is an artifact of the camera caused by the intense direct beam [cf. Fig. 3(c)]. A similar but somewhat weaker effect can be also seen in Fig. 14.

cantly deplete the direct beam towards the end of the long-range-ordered crystal. In an earlier paper [24] we have suggested that diffraction switches to the dynamic regime in the long-range ordered wet colloidal crystals. Figure 14 provides a direct confirmation of the dynamic character of diffraction even at higher x-ray energies (15 keV instead of 10 keV [23], the latter corresponding to a $1.5^2=2.25$ times higher refractive index contrast).

It is enlightening to compare the strength of the diffraction in the crystal after drying, when the extent of the positional order $\Lambda$ is significantly shortened. Figure 15 shows the diffraction pattern measured in the dry sample at exactly the same position and the same orientation. After drying the contrast is enhanced by about 80% so that the power scattered by one silica sphere is more than three times larger and $L_{(110)}^{\mathrm{dry}}=0.14$ mm. However, the diffracted intensity is seen to significantly reduce, mostly due to shortening of the crystal positional correlation length $\Lambda$ in Eq. (4), which significantly overcompensates the shortening of $L_{(110)}$. The pattern in Fig. 15 can be considered as an incoherent sum of kinematic diffraction patterns originating from small domains, which are positionally uncorrelated with each other.

We also note that, despite the contrast enhancement, the intensity of the direct beam was increased by about a factor of 2 so that a shorter exposure time $\Delta T$ was used to avoid detector saturation. In the dry crystal the absorption is practically unaffected since it is mostly originating from the silica spheres and the glass walls of the capillary. This reduction of the sample extinction is thus caused by the decrease of the diffraction strength. The results presented in Figs. 14 and 15 indicate that the strength of the diffraction and its transition into the dynamic regime can be used as an alternative approach to probe the extent of the positional order in colloidal crystals. Development of appropriate theory is, however, needed in order to exploit dynamic diffraction for a detailed quantitative characterization of the order parameters.

## VII. CONCLUSIONS

In this work we present the analysis of the requirements needed to observe coherent x-ray diffraction in colloidal crystals in a small-angle geometry. It is shown that in the longitudinal direction, i.e., along the beam propagation direction, a reciprocal space resolution of the order of $\delta q/k_0 \sim 10^{-6}$ can be achieved, which is sufficient to detect the presence of long-range positional order. The transverse resolution of the setup was improved here to about $\delta q/k_0 \sim 2\sigma/k_0=1.3\times 10^{-5}$, i.e., a factor 5–10 better than previously reported [19–24].

Furthermore, we have applied the high-resolution small-angle x-ray diffraction technique to observe *in situ* the modification of the crystal structure caused by capillary forces during drying. Broadening of the diffraction peaks is observed already when the meniscus reaches the sediment. We associate this with a stress field originating from capillary forces applied at the top of the sediment and elastically propagating down. When air penetrates into the sediment and a wet part of it is encapsulated by the solvent-air interface, the stress crosses a critical value and the crystal breaks into many domains with slightly different orientations. All structural changes observed are induced by external stress fields in the wet crystal and no change in its structure is detected when it finally dries.

We have also presented direct evidence of the dynamic regime of x-ray diffraction in the long-range-ordered colloidal crystal. However, the diffraction switches to the (nearly) kinematic regime when the long-range positional order is destroyed. Our results indicate that the strength of the diffraction and its transition into the dynamic regime can be used as an alternative approach to probe the extent of the positional order in photonic colloidal crystals.

## ACKNOWLEDGMENTS

This work was to a large extent inspired by Henk Lekkerkerker; his support and constructive criticism at all stages were essential. It is our pleasure to thank Xinyi Xian for her enthusiastic help during the experiment. Alfons van Blaaderen, Willem Kegel, Arnout Imhof, Judith Wijnhoven, and Wim Bras are thanked for fruitful discussions, and Nynke Verhaegh for particle synthesis. The Netherlands Organization for the Advancement of Research (NWO) is acknowledged for providing us with the possibility of performing measurements at DUBBLE.

[1] W.G. Hoover and F.H. Ree, J. Chem. Phys. **49**, 3609 (1968).
[2] P.N. Pusey and W. van Megen, Nature (London) **320**, 340 (1986).
[3] P.N. Pusey, W. van Megen, P. Bartlett, B.J. Ackerson, J.G. Rarity, and S. M Underwood, Phys. Rev. Lett. **63**, 2753 (1989).
[4] K. Schätzel and B.J. Ackerson, Phys. Rev. E **48**, 3766 (1993); B.J. Ackerson and K. Schätzel, *ibid.* **52**, 6448 (1995).
[5] J. Zhu, M. Li, R. Rogers, W. Meyer, R.H. Ottewill, STS-73

Space Shuttle Crew, W.B. Russel, and P.M. Chaikin, Nature (London) **387**, 883 (1997).
[6] J.L. Harland, S.I. Henderson, S.M. Underwood, and W. van Megen, Phys. Rev. Lett. **75**, 3572 (1995); J.L. Harland and W. van Megen, Phys. Rev. E **55**, 3054 (1997).
[7] R.L. Davidchack and B.B. Laird, Phys. Rev. Lett. **85**, 4751 (2000).
[8] Zh. Cheng, P.M. Chaikin, J. Zhu, W.B. Russel, and W.V. Meyer, Phys. Rev. Lett. **88**, 015501 (2002).
[9] J.P. Hoogenboom, A.K. van Langen-Suurling, J. Romijn, and A. van Blaaderen, Phys. Rev. Lett. **90**, 138301 (2003).
[10] S. Auer and D. Frenkel, Phys. Rev. Lett. **91**, 015703 (2003).
[11] A. Yethiraj and A. van Blaaderen, Nature (London) **421**, 513 (2003).
[12] S. Pronk and D. Frenkel, Phys. Rev. Lett. **90**, 255501 (2003).
[13] J.E.G.J. Wijnhoven and W.L. Vos, Science **281**, 802 (1998).
[14] A. Blanco *et al.*, Nature (London) **405**, 437 (2000).
[15] R. Rengarajan, P. Jiang, D.C. Larrabee, V.L. Colvin, and D.M. Mittleman, Phys. Rev. B **64**, 205103 (2001).
[16] Y.A. Vlasov, X.-Z. Bo, J.C. Sturm, and D.J. Norris, Nature (London) **414**, 289 (2001).
[17] K.P. Velikov, C.G. Christova, R.P.A. Dullens, and A. van Blaaderen, Science **296**, 106 (2002).
[18] R. E. Peierls, *Surprises in Theoretical Physics* (Princeton University Press, Princeton, NJ, 1979), see Chap. 4.1, pp. 85-91.
[19] W. Vos, M. Megens, C.M. van Kats, and P. Bosecke, Langmuir **13**, 6004 (1997).
[20] J.E.G.J. Wijnhoven, L. Bechger, and W.L. Vos, Chem. Mater. **13**, 4486 (2001).
[21] M. Megens and W.L. Vos, Phys. Rev. Lett. **86**, 4855 (2001). Note that the authors use scattering vector $s = q/2\pi$.
[22] H. Versmold, S. Musa, and A. Bierbaum, J. Chem. Phys. **116**, 2658 (2002).
[23] A.V. Petukhov, D.G.A.L. Aarts, I.P. Dolbnya, E.H.A. de Hoog, K. Kassapidou, G.J. Vroege, W. Bras, and H.N.W. Lekkerkerker, Phys. Rev. Lett. **88**, 208301 (2002).
[24] A.V. Petukhov, I.P. Dolbnya, D.G.A.L. Aarts, G.J. Vroege, and H.N.W. Lekkerkerker, Phys. Rev. Lett. **90**, 028304 (2003).
[25] A.F. Routh and W.B. Russel, Langmuir **15**, 7762 (1999).
[26] F.X. Redl, K.-S. Cho, C.B. Murray, and S. O'Brien, Nature (London) **423**, 968 (2003).
[27] N.A.M. Verhaegh and A. van Blaaderen, Langmuir **10**, 1427 (1994); N.A.M. Verhaegh, D. Asnagi, and H.N.W. Lekkerkerker, Physica (Amsterdam) **264A**, 64 (1999); E.H.A. de Hoog, L.I. de Jong-van Steensel, M.M.E. Snel, J.P.J.M. van der Eerden, and H.N.W. Lekkerkerker, Langmuir **17**, 5486 (2001).
[28] E.H.A. de Hoog, Ph.D. thesis, University of Utrecht, 2001.
[29] H. de Hek and A. Vrij, J. Colloid Interface Sci. **70**, 592 (1979).
[30] M. Borsboom *et al.*, J. Synchrotron Radiat. **5**, 518 (1998).
[31] J.V. Sanders, Acta Crystallogr., Sect. A: Cryst. Phys., Diffr., Theor. Gen. Crystallogr. **24**, 427 (1968).
[32] N.A.M. Verhaegh, J.S. van Duijneveldt, A. van Blaaderen, and H.N.W. Lekkerkerker, J. Chem. Phys. **102**, 1416 (1995).
[33] W.K. Kegel and J.K.G. Dhont, J. Chem. Phys. **112**, 3431 (2000).
[34] Ch. Dux and H. Versmold, Phys. Rev. Lett. **78**, 1811 (1997).
[35] J. Liu, D.A. Weitz, and B.J. Ackerson, Phys. Rev. E **48**, 1106 (1993).
[36] V.C. Martelozzo, A.B. Schofield, W.C.K. Poon, and P.N. Pusey, Phys. Rev. E **66**, 021408 (2002).
[37] S. Pronk and D. Frenkel, J. Chem. Phys. **110**, 4589 (1999).
[38] P.G. Bolhuis, D. Frenkel, S.-C. Mau, and D.A. Huse, Nature (London) **388**, 235 (1997).
[39] A.J.C. Wilson, Proc. R. Soc. London, Ser. A **180**, 277 (1941); *X-Ray Optics* (Methuen, London, 1949).
[40] See http://www.chem.uu.nl/fcc/drying, where one can find auxiliary material for Sec. V such as the evolution of the diffraction pattern and photos of the drying sample.
[41] M.D. Haw, M. Gillie, and W.C. Poon, Langmuir **18**, 1626 (2002).
[42] J.M. Polson, E. Trizac, S. Pronk, and D. Frenkel, J. Chem. Phys. **112**, 5339 (2000).
[43] D.A. Kofke and P.G. Bolhuis, Phys. Rev. E **59**, 618 (1999).
[44] W.G.T. Kranendonk and D. Frenkel, Mol. Phys. **72**, 679 (1991).
[45] S.R. Williams, I.K. Snook, and W. van Megen, Phys. Rev. E **64**, 021506 (2001).